# Morphological Changes of Silicon Nanoparticles and the Influence of Cutoff Potentials in Silicon-Graphite Electrodes

**Morten Wetjen,[1,*,z] Sophie Solchenbach,[1,*] Daniel Pritzl,[1,*] Jing Hou,[2] Vasiliki Tileli,[2] and Hubert A. Gasteiger[1,**]**

[1] *Chair of Technical Electrochemistry, Department of Chemistry and Catalysis Research Center, Technische Universität München, D-85748 Garching, Germany*
[2] *Institute of Materials, École Polytechnique Fédérale de Lausanne, CH-1015 Lausanne, Switzerland*

Silicon-graphite electrodes usually exhibit improved cycling stability when limiting the capacity exchanged by the silicon particles per cycle. Yet, the influence of the upper and the lower cutoff potential was repeatedly shown to differ significantly. In the present study, we address this discrepancy by investigating two distinct degradation phenomena occurring in silicon-graphite electrodes, namely (i) the roughening of the silicon particles upon repeated (de-)lithiation which leads to increased irreversible capacity losses, and (ii) the decay in the reversible capacity which mainly originates from increased electronic interparticle resistances between the silicon particles. First, we investigate the cycling stability and polarization of the silicon-graphite electrodes in dependence on different cutoff potentials using pseudo full-cells with capacitively oversized $LiFePO_4$ cathodes. Further, we characterize post-mortem the morphological changes of the silicon nanoparticles by means of scanning transmission electron microscopy (STEM) and energy dispersive spectroscopy (EDS) as a function of the cycle number. To evaluate the degradation of the entire electrode coating, we finally complement our investigation by impedance spectroscopy (EIS) with a gold-wire micro-reference electrode and post-mortem analyses of the electrode structure and coating thickness by cross-sectional SEM.
 [DOI: 10.1149/2.1261807jes]

Manuscript submitted February 23, 2018; revised manuscript received May 10, 2018. Published May 18, 2018. This was Paper 424 presented at the National Harbor, Maryland Meeting of the Society, October 1–5, 2017.

Silicon is among the most promising anode materials for future lithium-ion batteries.[1,2] For example, a prismatic hard case cell comprising a silicon-carbon anode with 1000 mAh $g^{-1}_{electrode}$ and an NMC811 cathode would offer a specific energy of up to ~280 Wh $kg^{-1}_{cell}$.[3] In contrast to state-of-the-art graphite electrodes, where lithium is inserted into the interlayers between the graphene sheets, silicon reacts with lithium and forms $Li_xSi$ alloys.[4–6] Because the (de-)alloying reaction allows a higher lithium uptake per silicon atom (3579 mAh $g^{-1}_{Si}$, $Li_{15}Si_4$) compared to the intercalation of lithium into the graphite host structure (372 mAh $g^{-1}_{C}$, $LiC_6$), silicon offers an about ~10 times larger theoretical specific capacity.[7] However, while the intercalation chemistry reveals excellent cycling stability with only minor irreversible changes of the graphite's morphology (ca. +10%),[8] the (de-)alloying reaction causes significant morphological and chemical changes to the silicon particles, including (i) a large volume expansion of up to +280% and (ii) repeated breakage and formation of Si-Si bonds, which leads to severe mechanical stress and particle fracturing.[9–12] Upon continued cycling, these morphological changes cause a rapid capacity decay of silicon-based electrodes, which is largely driven by the electrical isolation of the fractured silicon particles.[13–17] Nanometer-sized structures, including nanoparticles and nanowires, were shown to mitigate the mechanical stress which results from volumetric changes during the (de-)alloying reaction.[12,18–20] However, there exists a trade-off, because the reduction of the particle size also leads to a lower volumetric energy density and an inferior electrical conductivity across the electrode.[21,17] Possibly equally important and detrimental for the long-term stability of nanometer-sized silicon is its high specific surface area, which leads to a significantly increased irreversible capacity.[22]

Inspired by the early work on lithium-alloys in nonaqueous electrolyte solutions by Dey[23] and by Nicholson,[24] the coulombic efficiency and rate of the alloying reactions have been subject to numerous studies. Especially, lithium-alloys with silicon[25] and aluminum[26] attracted the interested of researchers because of their high specific capacity, good reversibility and mitigation of lithium dendrites. The morphological changes of silicon caused by (de-)alloying have been investigated, e.g., by means of in situ lab or synchrotron based X-ray diffraction (XRD),[27–30] nuclear magnetic resonance spectroscopy (NMR),[11,31–34] and in situ transmission electron microscopy (TEM),[12,35–38] which provided valuable insights into the phase transition of crystalline silicon as well as the volumetric expansion and strain-induced fracture of silicon particles within the first cycles. As pointed out by McDowell et al.,[13] most of the these studies either deal with the degradation of individual particles or investigate primarily the first few cycles. However, to derive implications for practical applications of silicon-based batteries, it is important to examine the degradation of silicon particles also as part of the entire electrode structure, by considering (i) the electronic interparticle resistances between silicon particles, (ii) the mechanical integrity of the electrode, (iii) the impact of repeated (de-)lithiation on the morphology of the silicon particles, as well as (iv) the electrolyte decomposition and solid-electrolyte-interphase (SEI) formation at the silicon/electrolyte interface over longer cycling periods.

In the present study, we investigate the degradation of silicon-graphite (SiG) electrodes with 35 wt% of silicon nanoparticles (particle length scales of ~200 nm) and an areal capacity of 1.7–1.8 mAh $cm^{-2}$. Based on our previous work,[39] where we differentiated two distinct degradation phenomena occurring in silicon-graphite electrodes, namely (i) the roughening of the silicon particles upon repeated (de-)lithiation which leads to increased irreversible capacity losses (furtheron described as silicon particle degradation), and (ii) the decay in the reversible capacity which mainly originates from increased interparticle contact resistances between the silicon particles (furtheron described as electrode degradation), we now focus on the underlying morphological changes of the silicon particles and of the electrode structure that occur upon repeated (de-)lithiation. Inspired by recent publications of the groups of Aurbach,[40] Abraham,[41] and Kobayashi,[42] who independently reported a significant difference in the cycling stability of silicon-based electrodes depending on a capacity or potential limitation either during lithiation or delithiation, we extend our analysis of the different degradation phenonema by two cutoff potential-limited cycling protocols. While it is widely accepted in the literature[8] that limiting the capacity of silicon reduces its degradation and irreversible capacity loss, the differences between limiting either the lower or the upper cutoff potential still require further understanding.

By use of scanning transmission electron microscopy (STEM) and energy dispersive spectroscopy (EDS), we investigate the morphology and chemical composition of the silicon particles post

*Electrochemical Society Student Member.
**Electrochemical Society Fellow.
[z]E-mail: morten.wetjen@tum.de

mortem after different number of charge-discharge cycles in a SiG//$LiFePO_4$ pseudo-full cell setup (i.e., with a capacitively largely oversized cathode of ~3.5 mAh $cm^{-2}$) and a fluoroethylene carbonate (FEC)-based electrolyte.[39] Combining the microscopic characterization with the electrochemical analysis of the cycling stability, the electrode polarization, and the irreversible capacity losses upon cycling allows us to correlate the morphological changes of the silicon particles and the electrode with the observed cycling stability of the SiG electrodes. Electrochemical impedance spectroscopy (EIS) and cross-sectional scanning electron microscopy (SEM) images further complement the discussion by providing additional information about the electrode impedance and the morphological changes of the entire electrode structure as a function of the cycle number. A fully (de-)lithiated SiG electrode (0.01–1.25 V vs. $Li^+$/Li, ~89% utilization of its theoretical capacity at a C-rate of 0.33 $h^{-1}$) is used as baseline in this study, the degradation of which will be compared to a lithiation-limited SiG electrode (0.05–1.25 V vs. $Li^+$/Li) and a delithiation-limited SiG electrode (0.01–0.65 V vs. $Li^+$/Li), both with a lower utiliztation of ~76% of their theoretical capacity at 0.33 $h^{-1}$. Finally, we conclude our analysis with a detailed discussion of the impact of the upper/lower cutoff potentials on the morphological changes of silicon nanoparticles and the integrity of the SiG electrode.

## Experimental

***Silicon-graphite (SiG) electrode preparation.—***Silicon-graphite (SiG) electrodes, consisting of 35 wt% silicon nanoparticles (~200 nm dimensions, Wacker Chemie AG, Germany), 45 wt% graphite (~20 μm, T311, SGL Carbon, Germany), 10 wt% vapor grown carbon fibers (VGCF-H, Showa Denko, Japan), and 10 wt% lithium poly(acrylate) binder (LiPAA) were prepared through an aqueous ink procedure, which is described in detail in our previous publication.[39] The LiPAA was prepared by diluting a 35 wt% poly(acrylic acid) solution (PAA, MW = 250,000 g $mol^{-1}$, Sigma-Aldrich, Germany) with deionized water and neutralizing it with lithium hydroxide (LiOH, Sigma-Aldrich, Germany) to a pH-value of ~8.[43] The theoretical areal capacity of these electrodes was 1.8–1.9 mAh $cm^{-2}$ (referenced to the theoretical specific capacities of 3579 mAh $g^{-1}{}_{Si}$ and 372 mAh $g^{-1}{}_{C}$, respectively, for the full potential range of 0.01–1.25 V vs. $Li^+$/Li), which corresponds to a mass loading of ~1.4 $mg_{electrode}$ $cm^{-2}$. Practically, first cycle delithiation capacities of 1.7–1.8 mAh $cm^{-2}$ (~1280 mAh $g^{-1}{}_{electrode}$) could be utilized at a C-rate of 0.1 $h^{-1}$. This discrepancy can be rationalized by considering Figure 1b which shows the potential profiles of the first cycle for the individual active materials at 0.05 $h^{-1}$ (viz., silicon:VGCF–H:LiPAA 37.5:37.5:25 wt% or graphite:LiPAA 95:5 wt%). The electrodes were prepared analogously to the procedure described above. Accordingly, the graphite electrode shows a first cycle delithiation capacity of 343 ± 2 mAh $g^{-1}{}_{C}$ (i.e., ~92% of the theoretical capacity of 372 mAh $g^{-1}$), while the silicon electrode delivers 3273 ± 16 mAh $g^{-1}{}_{Si}$ (i.e., ~91% of the theoretical capacity of 3579 mAh $g^{-1}{}_{Si}$). By considering a small capacity contribution of the carbon fibers (~80 mAh $g^{-1}{}_{VGCF}$),[48] the practical capacity utilization of silicon shrinks to ~89%. Transferring these values to the SiG electrodes results in an accessible electrode capacity of 1277 mAh $g^{-1}{}_{electrode}$, which is in a good agreement with the practical first cycle delithiation capacity of ~1280 mAh $g^{-1}{}_{electrode}$. As a corollary, about ~11 wt% of the silicon nanoparticles do not contribute the reversible capacity, likely because of the formation of electrochemically inactive $SiO_2$ during the aqueous ink procedure.

***Test cell assembly.—***Electrochemical characterization was performed in Swagelok T-cells (Swagelok, Germany), incorporating a lithiated gold-wire micro-reference electrode as described in detail by Solchenbach et al.[44] For post-mortem characterization of the SiG electrodes via STEM and SEM, CR2032 coin-cells (Hohsen, Japan) were prepared using the same electrode configuration. All cells were assembled in an Ar atmosphere MBraun glove box ($H_2O$ and $O_2$ concentration <0.1 ppm), by sandwiching two porous glass fiber separators (thickness 250 μm, VWR, USA) that were soaked with electrolyte solution between a silicon-graphite anode (1.7–1.8 mAh $cm^{-2}$ at 0.1 $h^{-1}$) and a capacitively oversized $LiFePO_4$ (LFP) cathode (3.5 mAh $cm^{-2}$, Custom cells, Germany). As electrolyte solution, a mixture of 1 M $LiPF_6$ in ethylene carbonate:ethyl methyl carbonate (EC:EMC, 3:7 w:w) with 5 wt% fluoroethylene carbonate (FEC) was used. Capacitively oversized LFP electrodes were selected for three reasons: (i) a capacitively oversized LFP cathode excludes the loss of active lithium as cause for cell polarization for the number of cycles conducted in this work; (ii) LFP forms a potential plateau at about 3.45 V vs. $Li^+$/Li during (de-)lithiation, which was used to reference the SiG electrode potential to the $Li^+$/Li potential; and, (iii) the low potential of the LFP cathode minimizes detrimental side reactions between the electrolyte and the cathode.[39]

***Battery cycling.—***The electrode polarization and cycling performance of the SiG electrodes was investigated by constant current cycling of SiG//LFP Swagelok T-cells. The C-rate was always referenced to the full theoretical capacity, independent of the cutoff potential (i.e., a C-rate of 1.0 $h^{-1}$ corresponds to 1.8–1.9 mA $cm^{-2}$). The cell voltage was controlled between the silicon-graphite and the LFP electrode, whereby the SiG potential was calculated from the SiG//LFP cell voltage, based on the constant LFP potential of 3.45 V vs. $Li^+$/Li for the here used capacitively oversized LFP electrode. Initially, two formation cycles were performed of all electrodes between 0.01–1.25 V vs. $Li^+$/Li at a low C-rate of 0.1 $h^{-1}$ (~0.2 mA $cm^{-2}$) to achieve a similar passivation. The data of these first two cycles are omitted from the following figures and cycle number one in cycle-life tests refers to the first cycle after these initial two formation cycles. Cycle life tests at a C-rate of 0.33 $h^{-1}$ (~0.6 mA $cm^{-2}$) were conducted using three different voltage ranges: (i) full lithiation/delithiation between 0.01–1.25 V vs. $Li^+$/Li, (ii) partial lithiation between 0.05–1.25 V vs. $Li^+$/Li (furtheron referred to as lithiation-limited), and (iii) partial delithiation between 0.01–0.65 V vs. $Li^+$/Li (furtheron referred to as delithiation-limited). Every 1$^{st}$, 32$^{nd}$, and 63$^{rd}$ cycle (after formation), one cycle was applied to all electrodes in the full potential range: starting from the upper cutoff potential of the preceding cycle, the SiG electrodes were first lithiated to 0.01 V vs. $Li^+$/Li at 0.1 $h^{-1}$ (~0.2 mA $cm^{-2}$) and then delithiated to 2.0 V vs. $Li^+$/Li at 0.02 $h^{-1}$ (~0.04 mA $cm^{-2}$), before switching back to the respective set cutoff potentials and the higher C-rate of 0.33 $h^{-1}$. All measurements were performed in a climate chamber (Binder, Germany) at 25°C (±0.1°C), using either a battery cycler (Series 4000, Maccor, USA) or in case of the impedance measurements a multi-channel potentiostat VMP3 (BioLogic, France).

***Electrochemical impedance spectroscopy.—***Impedance measurements were performed during the slow intermediate cycles (1$^{st}$, 32$^{nd}$, and 63$^{rd}$), using the lithiated gold-wire micro-reference electrode of the Swagelok T-cell setup described above.[44] Hence, the SiG electrodes were first delithiated to 0.65 V vs. $Li^+$/Li (~15% SOC) and kept at this potential for 30 min by applying a constant voltage step. Afterwards, potentiostatic electrochemical impedance spectroscopy (PEIS) was measured in the frequency range of 100 kHz – 500 mHz, using a perturbation of 15 mV.

***Transmission electron microscopy.—***The morphology and relative composition of the silicon particles from an uncycled electrode and after 1, 5, 20, 40, and 60 cycles was investigated by scanning transmission electron microscopy (STEM) and energy dispersive spectroscopy (EDS), using a FEI Titan Themis (FEI, USA) at 200 kV. Prior to these measurements, the SiG electrodes were slowly delithiated at 0.02 $h^{-1}$ to 2.0 V vs. $Li^+$/Li, then harvested from the cells and carefully washed with 50 μL dimethyl carbonate (DMC), and finally dried in an inert atmosphere. Afterwards, the coatings were scratched and a TEM lacey carbon Cu 200 grid (EMS, USA) was directly pressed onto the surface to collect the powder before being

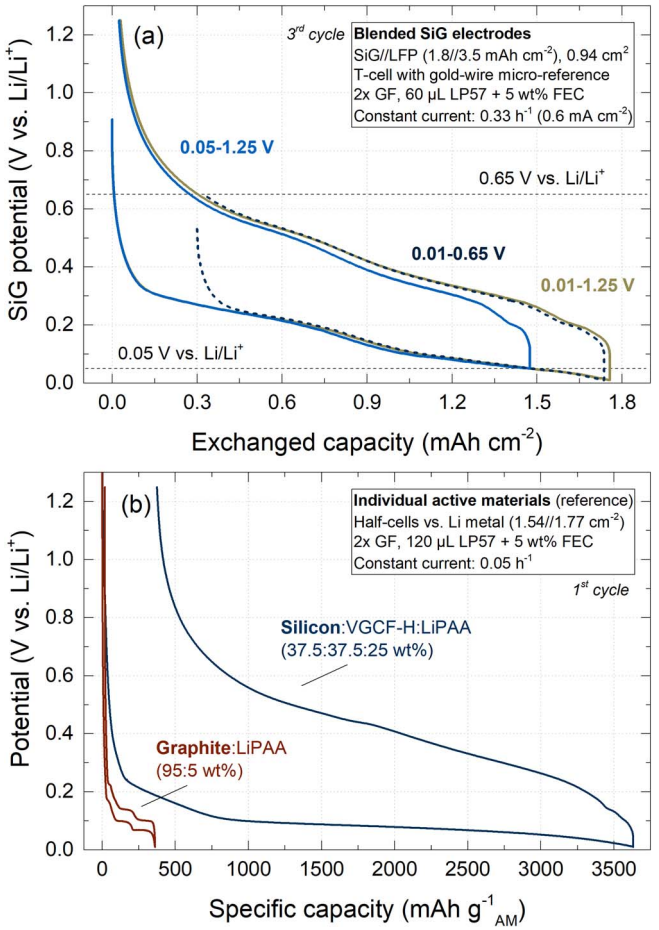


**Figure 1.** (a) Potential profiles of silicon-graphite electrodes vs. capacity during galvanostatic cycling at 0.33 $h^{-1}$ (3rd cycle) of SiG//LFP Swagelok T-cells at different cutoff potentials: 0.01–1.25 V vs. $Li^+$/Li (brown), 0.05–1.25 V vs. $Li^+$/Li (blue), and 0.01–0.65 V vs. $Li^+$/Li (marine). The SiG potential was calculated from the SiG//LFP cell voltage, based on the constant LFP potential of 3.45 V vs. $Li^+$/Li for the here used capacitively oversized LFP electrodes. (b) Potential profiles of the individual active materials during the first galvanostatic cycle at 0.05 $h^{-1}$ in half-cells against lithium metal between 0.01–1.25 V vs. $Li^+$/Li (marine: silicon/VGCF-H/LiPAA 37.5/37.5/25 wt%, red: graphite/LiPAA 95:5 wt%).

transferred into the instrument. During that period, the samples were exposed to air for a time interval of ∼10 min.

***Scanning electron microscopy.—***The morphology of the SiG electrodes prior to cycling and after 60 cycles at different cutoff potentials was investigated by cross-sectional scanning electron microscopy (SEM). First, electrode cross-sections were prepared by Argon ion beam polishing, using a JEOL Cross Section Polisher IB-09010CP (JEOL, Japan). Afterwards, SEM images were measured by use of a JEOL JSM-IT100 (JEOL, Japan) with a tungsten electron source and a secondary electron detector. Both the preparation of the cross-sections and the subsequent measurement of the SEM images were conducted by the JEOL (Germany) GmbH in Freising, Germany. Prior to the measurement, the samples were exposed to ambient atmosphere for less than an 30 minutes.

***Quantification of electrode thickness changes.—***The changes in the electrode thickness were measured by cross-sectional SEM with the aid of a JEOL JCM-6000 Neoscope (JEOL, Japan), using a modification of the method described by Mittermeier et al.[45] For each cutoff condition, two SiG//LFP coin-cells were aged for 60 cycles, using the same cycling procedure as described above, yet without the intermediate cycles at low C-rate. Afterwards, the SiG electrodes were harvested from the cells and embedded into a resign solution with a hardener, hereupon evacuated repeatedly in a desiccator to remove gas bubbles, and subsequently dried in an oven at 40°C overnight. The solid polymer block was then polished stepwise to obtain a mirror finished cross-section. For each cutoff condition, two electrodes were evaluated at fifteen positions along the entire cross-section, resulting in ∼30 measurements to obtain an average thickness and its standard deviation (represented by the error bars).

## Results and Discussion

***Influence of the cutoff potentials on the electrochemical performance of SiG electrodes.—***Figure 1a shows the potential profiles of the silicon-graphite (SiG) electrodes at different cutoff potentials during the 3rd cycle at 0.33 $h^{-1}$. Full (de-)lithiation of the electrodes between 0.01 and 1.25 V vs. $Li^+$/Li (brown line) provides a reversible capacity of ∼1.7 mAh $cm^{-2}$ at 0.33 $h^{-1}$ which corresponds to a capacity utilization of ∼89% (referenced to the theoretical value of ∼1.9 mAh $cm^{-2}$ for this electrode). The sloped profile of the potential curves shown in Figure 1a is characteristic for the (de-)lithiation of amorphous silicon, which contributes most of the electrode's capacity (∼88% based on the theoretical capacities, graphite accounts for ∼12%). While the formation of the lithium-graphite compounds $LiC_x$ starts not until potentials below 0.19 V vs. $Li^+$/Li and is therefore largely overlapped by the lithiation of silicon, it can be distinguished during the delithiation process by the small plateau at potentials below 0.24 V vs. $Li^+$/Li (see Figure 1a).[39] By limiting either the lithiation to 0.05 V vs. $Li^+$/Li (blue line) or alternatively the delithiation to 0.65 V vs. $Li^+$/Li (dashed marine line), the reversible capacity at 0.33 $h^{-1}$ drops to a similar value of ∼1.45 mAh $cm^{-2}$, i.e., to ∼76% of the theoretical capacity. It is noted that a partial delithiation presupposes a previous full lithiation of the SiG electrode, which means that at least 0.25 mAh $cm^{-2}$ (∼15%) excess capacity remains in the electrode.

Obrovac and Christensen demonstrated that limiting the lithiation of silicon-based electrodes to potentials above 0.05 V vs. $Li^+$/Li avoids the formation of the metastable crystalline $Li_{15}Si_4$ phase and results in a better cycling performance due to the absence of the two-phase reaction of crystalline $Li_{15}Si_4$ to amorphous $Li_{\sim 2}Si$, which has been associated with detrimentally high internal stress in the silicon particles.[7] For the here investigated SiG electrodes, we observed the characteristic delithiation plateau of the $Li_{15}Si_4$ phase around 0.45 V vs. $Li^+$/Li only during the two formation cycles at a low C-rate of 0.1 $h^{-1}$ (data not shown). However, during subsequent cycling at a higher C-rate of 0.33 $h^{-1}$ (see Figure 1a) the feature disappeared, indicating that $Li_{15}Si_4$ formation did not occur at the here applied C-rate at any of the investigated cutoff potentials.[16] The reason for this lies in the high overpotential of the SiG electrodes during lithiation, which prevents the formation of the $Li_{15}Si_4$ phase at the expense of lowering the achievable capacity. If, on the other hand, as in our previous study with the same SiG electrodes,[39] a constant potential hold step at 0.01 V vs. $Li^+$/Li is applied, a distinct peak at about 0.45 V vs. $Li^+$/Li can be observed during delithiation even upon continued cycling. Therefore, we conclude that the following results recorded without potential hold are not influenced by additional stress arising from the $Li_{15}Si_4$ two-phase boundary at potentials below 0.05 V vs. $Li^+$/Li.

Figure 2 shows (a) the coulombic efficiency (defined as the first cycle delithiation capacity divided by the first cycle lithiation capacity) and (b) the areal delithiation capacity of the SiG electrodes at different cutoff potentials as a function of the cycle number. The delithiation capacity reveals a distinct decay within the first 60 cycles, which occurs not only during full (de-)lithiation (brown symbols) but also during the lithiation-limited cycling (blue symbols), i.e., during the two cycling conditions at which the electrodes are nominally fully delithiated to 1.25 V vs. $Li^+$/Li. As recently reported by Yoon et al.,[15] this decay can be associated with the degradation of the SiG electrode and is caused by the buildup of interfacial resistances (electronic and/or charge transfer resistances) for upper cutoff voltages which allow for a complete delithiation of the silicon. In contrast,

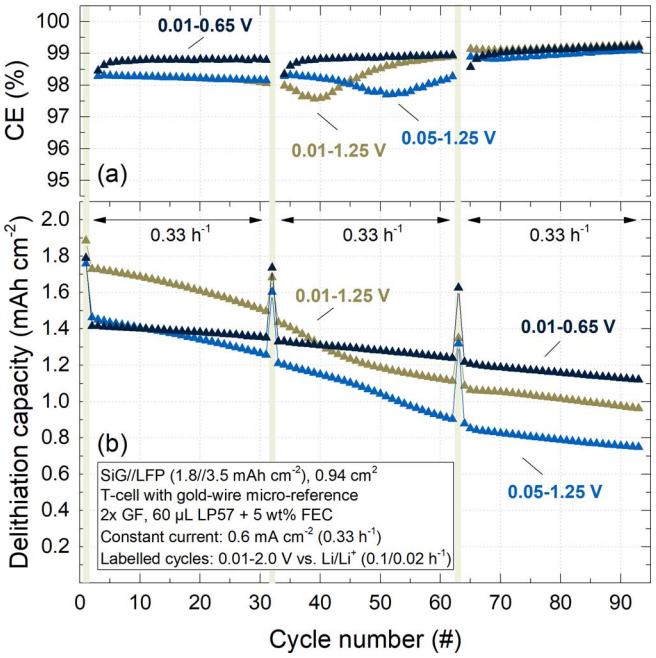


**Figure 2.** (a) Coulombic efficiency and (b) delithiation capacity obtained from constant current cycling (0.33 $h^{-1}$) of SiG//LFP Swagelok T-cells at different cutoff potentials: 0.01–1.25 V vs. $Li^+$/Li (brown), 0.05–1.25 V vs. $Li^+$/Li (blue), and 0.01–0.65 V vs. $Li^+$/Li (marine). The yellow bars indicate intermediate cycles (1st, 32nd, and 63rd), which were performed at lower C-rates (lithiation: 0.1 $h^{-1}$, delithiation: 0.02 $h^{-1}$) and the capacities of which are summarized in Table I; for these single cycles evaluation of the coulombic efficiency is not meaningful and is thus not shown.

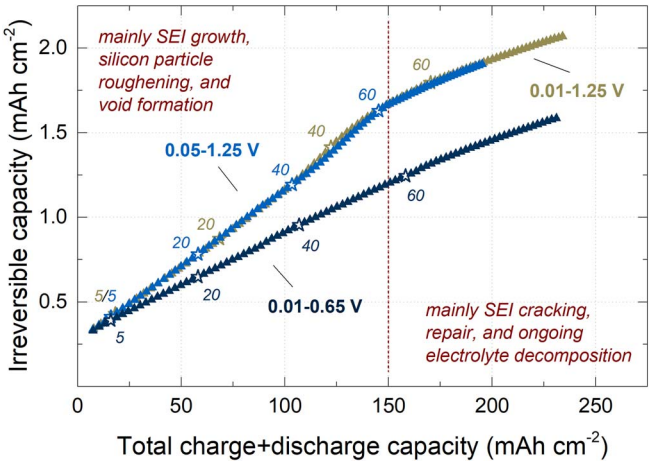


**Figure 3.** Total irreversible capacity $\sum Q_{irr}$ (in mAh $cm^{-2}$) of silicon-graphite electrodes as a function of the total exchanged charge+discharge capacity (in mAh $cm^{-2}$), obtained from the constant current cycling data of the SiG//LFP (1.8//3.5 mAh $cm^{-2}$) Swagelok T-cells shown in Figure 2 (i.e., over 90 cycles at 0.33 $h^{-1}$). The irreversible capacity contribution from the intermediate cycles (0.1/0.02 $h^{-1}$) were omitted to mitigate the influence of the different C-rates. The hollow stars label the number of the respective charge-discharge cycles. Electrolyte: LP57 + 5 wt% FEC.

for delithiation-limited SiG electrode cycling (0.01–0.65 V; marine symbols), only a comparatively small capacity fade upon cycling is observed. In this case, ~15% (~0.25 mAh $cm^{-2}$) of active lithium remain in the silicon, which according to Kimura et al.[42] reduces the formation of electronically insulated silicon particles. We would like to stress that although the capacity contribution from graphite is likely smaller for the lithiation-limited electrode (0.05–1.25 V; blue symbols), a similar behavior was also reported in the literature for silicon-based electrodes which did not contain any graphite.[40,42]

Next, we wanted to understand whether the improved cycling stability at the delithiation-limited cutoff potential results really from an improved electrode integrity and decreased overpotential or results just from a reduced lithium immobilization in poorly connected silicon particles due to the deliberate incomplete lithiation. Hence, the delithiation capacity of the intermediate cycles which were performed similarly for all electrodes in the full potential range with a deep delithiation (0.01–2.0 V vs. $Li^+$/Li) at very low C-rates is summarized in Table I. The delithiation-limited electrode reveals a high capacity retention of ≥91% even after 60 cycles, whereas the electrodes that were delithiated to 1.25 V vs. $Li^+$/Li demonstrate only a residual reversible capacity of 72–75%. Therefore, these results demonstrate that at the selected cycling conditions a higher upper cutoff potential not only reduces the cycling stability of the SiG electrode (irrespective of the overall exchanged capacity), but also lowers the amount of cyclable lithium due to the formation of inaccessible lithium. Note that the capacitively largely oversized LFP cathode provides a non-limiting lithium inventory in the cell and remains at a stable reference potential of 3.45 V vs. $Li^+$/Li with only a marginal potential upward shift of 20–25 mV over the examined ~100 cycles. Considering the potential profiles shown in Figure 1a, this corresponds to a reversible capacity loss of 0.1–0.2 mAh $cm^{-2}$ for each of the cutoff conditions. As a corollary, we slightly underestimate the residual capacity of our SiG electrodes after 100 cycles compared to measurements in half-cells.

The coulombic efficiency of the SiG electrodes shown in Figure 2a further supports the observation that electrodes which were delithiated to 1.25 V vs. $Li^+$/Li (brown and blue symbols) behave more alike than electrodes that were cycled at the same reversible capacity but at different cutoff potentials (blue and marine symbols). Clearly, the delithiation-limited electrode (marine symbols) indicates on average a 0.7% higher coulombic efficiency within the first 60 cycles, which increases steadily upon cycling. In contrast, the fully delithiated electrodes (brown and blue symbols) do not only start at a lower value of 98.3% but also show a slight decline during the same period that is followed by a minimum at ~97.7% after 40 cycles for the full (de-)lithiation (brown symbols) and after 50 cycles during the lithiation-limited cycling (blue symbols), respectively. After 60 cycles, however, a rapid increase can be observed in the coulombic efficiency across all cutoff potentials, which results in a similar value of 99.2% after 90 cycles for all electrodes.

To understand the origin of the differences in the coulombic efficiency when cycling with different cutoff potentials, Figure 3 illustrates the total irreversible capacity, i.e., the summation of the irre-

**Table I. Delithiation capacity and capacity retention of selected intermediate cycles performed at a lower cutoff potential of 0.01 V vs. Li/Li at a lithiation rate of 0.1 $h^{-1}$ and a deep delithiation to 2.0 V vs. $Li^+$/Li at delithiation rate of 0.02 $h^{-1}$.**

| | Delithiation capacity/mAh $cm^{-2}$ | | | Capacity retention/% | |
|---|---|---|---|---|---|
| Cutoff potentials | 1st cycle | 32nd cycle | 63rd cycle | cycle 1–32 | cycle 1–63 |
| 0.01–1.25 V (full (de-)lithiation) | 1.88 | 1.68 | 1.35 | 89 | 72 |
| 0.05–1.25 V (lithiation-limited) | 1.76 | 1.60 | 1.32 | 91 | 75 |
| 0.01–0.65 V (delithiation-limited) | 1.79 | 1.74 | 1.62 | 97 | 91 |

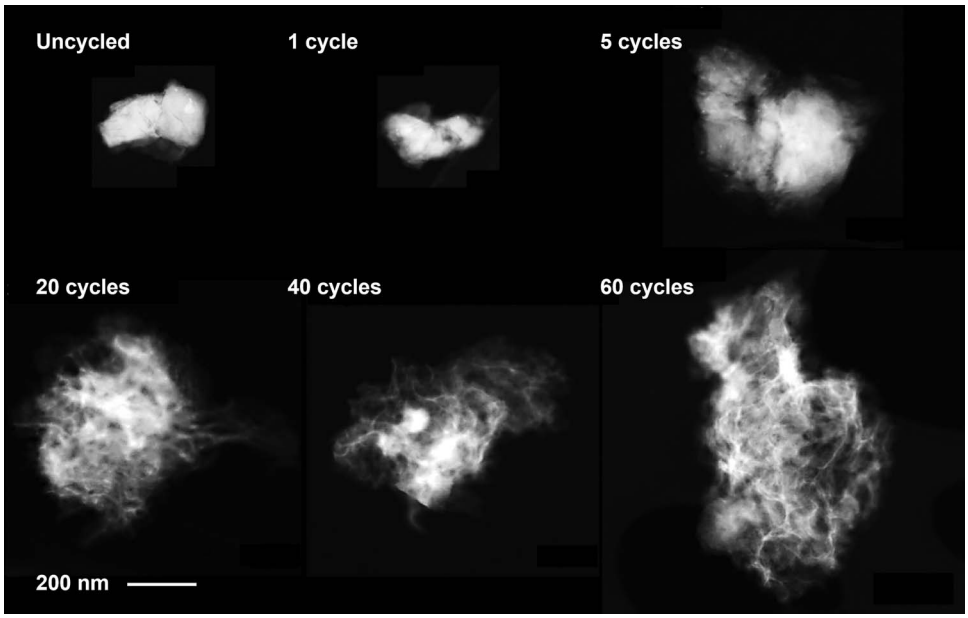


**Figure 4.** Scanning transmission electron microscopy (STEM) images of silicon particles from an uncycled electrode (upper left panel) and after different number of full (de-)lithiation cycles using the standard cutoff potentials of 0.01–1.25 V vs. $Li^+/Li$ (1, 5, 20, 40, and 60 cycles; 60 cycles corresponds to a total charge+discharge capacity of ∼170 Ah $cm^{-2}$ in Figure 3). High-angle annular dark field (HAADF) detector, acceleration voltage: 200 kV.

versible capacity for each cycle, as a function of the total exchanged charge+discharge capacity. In contrast to plotting the accumulated irreversible capacity vs. the cycle number, plotting it vs. the total exchanged capacity takes into account the differences in the reversible capacity obtained over the different charge/discharge protocols, and allows thus to better compare the effect of the different cutoff potentials. Furthermore, for the interpretation of Figure 3 it is important to note that the irreversible capacity can almost be fully ascribed to the silicon particles, because graphite is almost completely passivated after the two formation cycles preceding the charge/discharge cycling test, so that its contribution to the accumulated irreversible capacity after formation is negligible compared to silicon.[39]

Two distinct slope regions can be differentiated in Figure 3 (see red dashed vertical line), very distinct for the electrodes that were delithiated to 1.25 V vs. $Li^+/Li$ (brown and blue symbols), and somewhat less pronounced for the delithiation-limited electrodes delithiated to 0.65 V vs. $Li^+/Li$ (marine symbols). The steep increase of the irreversible capacity within the first 60 cycles was previously ascribed to an enhanced growth of the solid-electrolyte-interphase (SEI) due to silicon particle roughening and void formation.[39] After ∼60 cycles, however, the curves become much flatter, which we interpreted to indicate that a steady-state silicon particle morphology was reached, so that the lower rate of irreversible capacity gains would result mainly from SEI cracking and electrolyte decomposition caused by the ongoing volumetric changes upon repeated (de-)lithiation.[39] In this latter stage of aging (i.e., after ∼60 cycles), the total irreversible capacity gain rate vs. total exchanged capacity of the electrodes delithiated to 1.25 V vs. $Li^+/Li$ (brown and blue symbols) approaches the same value (i.e., the flatter slope) of the delithiation-limited electrodes (marine symbols). In order to verify that this persists over more than the 90 cycles shown in Figure 3, we also performed an extended cycling procedure up to 150 cycles (data not shown), which confirmed that the total irreversible capacity gain rates at the different cycling conditions indeed converge to nearly identical values after 60–80 cycles. In other words, after ∼60 cycles, the coulombic efficiency shows only a minor dependence on the investigated cutoff potentials (see Figure 2a). From this point onwards, ongoing SEI cracking and renewal only depends on the amount of charge which is exchanged by the silicon particles upon cycling.

***Silicon particle degradation upon repeated (de-)lithiation.—*** Throughout our previous studies on SiG electrodes[39,46] as well as in the literature,[32,41,43,47] it has been observed that electrodes based on silicon nanoparticles typically show a significantly lower coulombic efficiency in comparison to conventional graphite. However, it can often be seen that the coulombic efficiency upon extended cycling goes through a minimum between ∼20–80 cycles before recovering to higher values again (see Figure 2a and references[39,43,48]). Our explanation for this phenomenon is that the silicon nanoparticles undergo dealloying reactions during the extraction of lithium, which result in a roughening of the particle surface and formation of void spaces, as recently shown for tin.[49] Dealloying is a common corrosion process which involves the selected dissolution of the more electrochemically active element, here lithium, from an alloy and results in the formation of a nanoporous structure of the more noble alloy constituent, here silicon.[50,51] The resulting surface area increase drives further electrolyte decomposition and SEI growth on the freshly exposed silicon/electrolyte interface, which results in the steeper increase of the irreversible capacity (compare Figure 3). To confirm our hypothesis, we aged SiG electrodes for a different number of cycles, using the standard cutoff potentials of 0.01–1.25 V vs. $Li^+/Li$ (see brown curve in Figure 2). Afterwards, we slowly delithiated the electrodes to ∼2.0 V vs. $Li^+/Li$ to extract any residual lithium from the active materials and prepared lacey carbon TEM grids as described in the Experimental section. Figure 4 shows representative STEM images of a silicon particle from an uncycled electrode and of aged silicon particles after 1, 5, 20, 40, and 60 cycles.

Prior to cycling, the silicon particles reveal an irregular shape, consisting of a dense, crystalline structure with a mean size of ∼200 nm (see top left panel). After the first cycle (top center panel), the shape and the dimensions remain very similar, whereas the silicon surface is less smooth and the edges are less defined, suggesting an amorphous structure without crystalline order and with a decreased density. From the literature it is known that crystalline silicon becomes amorphous upon the insertion of lithium and the formation of $Li_xSi$ alloys; only at high degrees of lithiation a metastable crystalline $Li_{15}Si_4$ phase is formed.[7] During the subsequent extraction of lithium, the resulting silicon phase remains amorphous and no crystalline phases are observed anymore if silicon is either cycled at potentials above 0.05 V vs. $Li^+/Li$

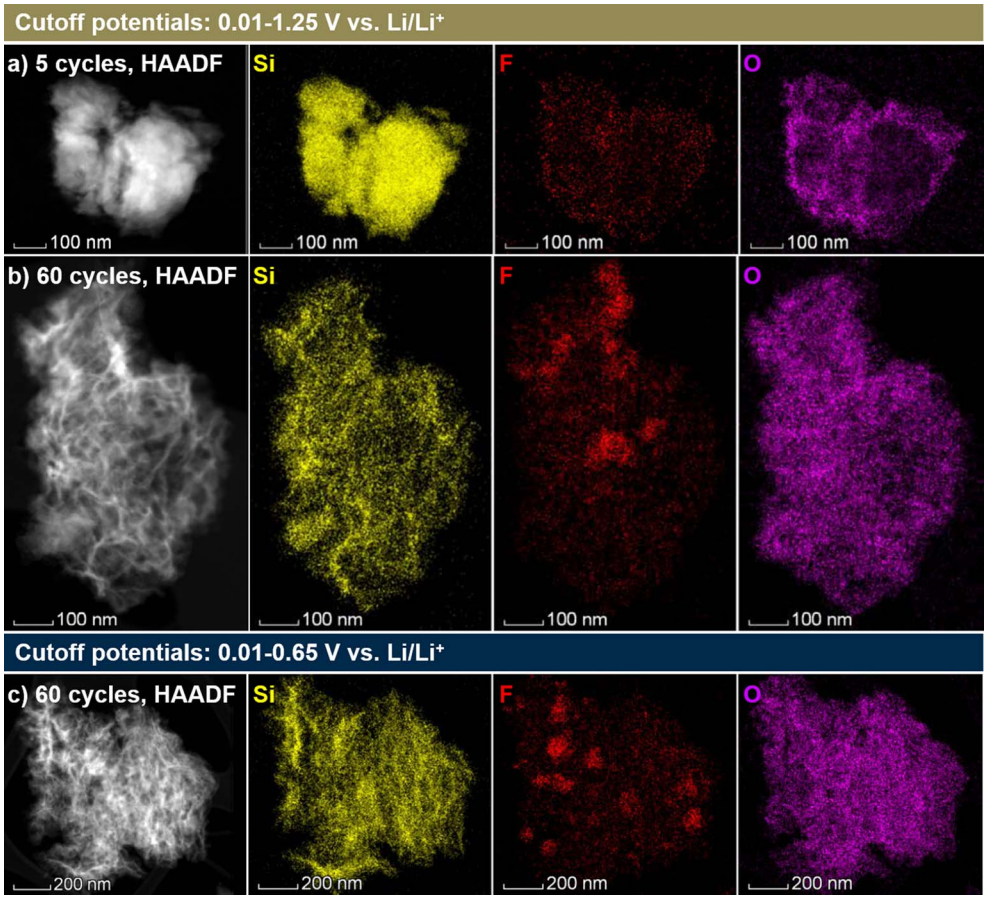


**Figure 5.** HAADF images and EDS spectra of the silicon particles, obtained after cycling to different cutoff potentials: 0.01–1.25 V vs. $Li^+/Li$ a) after 5 and b) after 60 cycles (particles as shown in Figure 4); and, c) 0.01–0.65 V vs. $Li^+/Li$ after 60 cycles. From left to right: HAADF image (white) and EDS spectra of silicon (yellow), fluorine (red), and oxygen (purple). Carbon was not considered, because the silicon particles were prepared on TEM carbon grids, which contributes significantly to the measurement.

or, as is the case in the present study, an increased electrode overpotential suppresses the formation of the $Li_{15}Si_4$ phase even at lower cutoff voltages of 0.01 V vs. $Li^+/Li$. Although the silicon particles undergo a large volume expansion up to +280% during the insertion of lithium, our STEM investigation indicates that after the first cycle the silicon particles return almost entirely to their initial dimensions in their delithiated state, with only minor deviation from the appearance of the uncycled silicon particle, which is in agreement with previous in situ atomic force microscopy measurements by Beaulieu et al.[52] However, Figure 4 also demonstrates that after 5 (top right panel) and even more after 20 cycles (bottom left panel), the silicon particles transform into an increasingly nanoporous structure with a high surface area and large void spaces, resulting in a considerable expansion with mean diameters up to 400 nm (in their delithiated state), which corresponds to a permanent volume expansion of approximately +700% (estimated from the ~2-fold expansion in each dimension). These morphological changes are accompanied by the formation of a continuous network of nanometer-sized silicon branches, which is presumably driven by a phase separation process at the solid/electrolyte interface, as described by Erlebacher et al.[50,53] The appearance of the silicon particles after 20 and more cycles (bottom panels of Figure 4) very much resembles the structures obtained upon the delithiation of Li–Sn alloys reported by Chen and Sieradzki.[49] Comparing the STEM images for 20, 40, and 60 cycles, one can notice that the change in the morphology of the silicon particles become less and less significant with increasing cycle number.

The progressive and large increase of the silicon surface area and the associated electrolyte decomposition at the newly formed silicon/electrolyte interface also explains the steep increase of the accumulated irreversible capacity over the first 60 cycles shown in Figure 3. Nonetheless, as indicated by the gradual decrease of the accumulated irreversible capacity gain rate (i.e., the slope in Figure 3) after ~60 cycles, the expansion of the silicon matrix by the dealloying process seems to approach a steady-state. Accordingly, the bottom center and right panel in Figure 4 show that already existing nanometer-sized silicon branches indicate less dramatic changes after 40 and 60 cycles, while few remaining dense areas expand further to also form a nanoporous silicon network. This can be explained by the fact that the increase of the silicon particle surface area and porosity leads to a decrease of the effective surface-normalized current density, which lowers the driving force for the formation of finer silicon filaments, as it was shown for Li–Sn alloys.[49] In other words, the morphological changes caused by dealloying of the silicon particles diminish their own root cause, namely the internal stress resulting from the repeated insertion and extraction of lithium.

Although the high-angle annular dark-field (HAADF) images shown in Figure 4 suggest that the silicon particles continuously transform into a continuous network of nanometer-sized highly branched silicon filaments, these structures are indeed not hollow. Instead, the freshly exposed silicon surface formed by these morphological changes of the silicon particles results in a further decomposition of electrolyte compounds at the silicon/electrolyte interface, leading to SEI growth and concomitant filling of the porous silicon structure. In fact, it is likely that the porous silicon structure is additionally stabilized by the SEI precipitates, which counteract the contraction of the high-surface area silicon structures during delithiation steps. Figure 5 shows the energy dispersive spectroscopy (EDS) spectra of silicon (yellow), fluorine (red), and oxygen (purple) of silicon

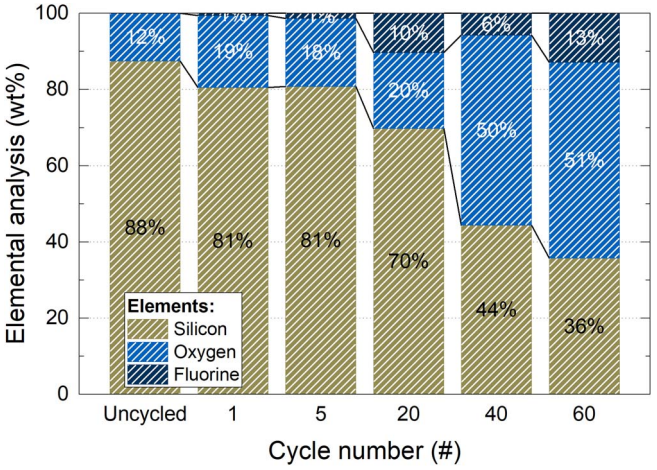


**Figure 6.** Relative weight composition determined by EDS analysis of silicon particles from uncycled electrodes and after different number of full (de-)lithiation cycles between 0.01–1.25 V vs. $Li^+$/Li, based on the data shown in Figure 4 and Figures 5a/5b.

particles (a) after 5 and (b) after 60 deep (de-)lithiation cycles between 0.01–1.25 V vs. $Li^+$/Li. The silicon spectrum (yellow) confirms the considerable decrease of the density of silicon within the expanded silicon particles and the formation of a nanoporous network upon cycling, whereas the fluorine and oxygen spectra reveal an inverse trend. Accordingly, only minor amounts of fluorine and oxygen can be seen after 5 cycles (panel a) at the edges of the particles, which mainly stem from the initial SEI formation and, in the case of oxygen, also from the initial native $SiO_2$ and additional $SiO_2$ formed during the aqueous ink processing. After 60 cycles (panel b), however, the spectra indicate much larger amounts of fluorine and oxygen that penetrate the entire nanoporous silicon structure.[54,55]

Figure 6 summarizes the relative weight composition of the silicon particles from uncycled electrodes and after different number of cycles. The uncycled particles show mostly silicon (~88 wt%) and small amounts of oxygen (~12 wt%). Considering that about 11% of the theoretical capacity of silicon are not accessible, likely because of $SiO_2$ which forms during the aqueous ink procedure, this would correspond to a silicon:oxygen mass ratio of 94:6 wt%. As a corollary, the oxygen content for the here investigated particles is slightly higher compared to values obtained by the electrochemistry for the entire electrode. Yet, given the sample size of few individual particles as well as the accuracy of EDS they are in a reasonable agreement. After several charge-discharge cycles, the relative contribution from silicon decreases continuously at the expense of larger amounts of the electrolyte decomposition products (here represented by fluorine and oxygen). In agreement with the increasing porosity within the silicon particle shown by the HAADF images (Figure 4 and Figure 5b), silicon accounts for only one third of the entire structure after 60 cycles. This number can be easily rationalized based on the electrolyte decomposition during the same period. Taking into account a total irreversible capacity loss of 1.79 mAh $cm^{-2}$ after 60 cycles (marked for the brown curve in Figure 3), which is mainly caused by the reductive decomposition of FEC ($M_W$ = 106.05 g $mol^{-1}$) and follows a four-electron reduction mechanism (i.e., 9.4 $\mu mol_{FEC}$ $mAh^{-1}$), as indicated by our previous electrolyte consumption studies using $^{19}$F-NMR,[39,48] the total amount of the reduced FEC amounts to 1.78 $mg_{FEC}$ $cm^{-2}$. Assuming as a zero order approximation that all FEC decomposition species transform into SEI products as well as considering further that fluorine and oxygen contribute about 57% to the molecular mass of FEC (i.e., 0.57 × 1.78 mg $cm^{-2}$) and that the initial silicon mass loading of the electrodes was ~0.5 $mg_{Si}$ $cm^{-2}$ (=0.35 × 1.4 mg $cm^{-2}$), the relative weight contribution of silicon after 60 cycles would be roughly 33 wt% and is thus in good agreement with the EDS spectra. Therefore, both the NMR and STEM investigation consistently demonstrate that the silicon-graphite electrodes are increasingly filled by electrolyte decomposition products, which do not only cover the active materials but also penetrate the increasingly nanoporous structure of the silicon particles.

After this discussion of the morphological transformation of the silicon particles upon extended deep delithiation to 1.25 V, the open question is whether this can also be observed under delithiation-limited condition, i.e., upon extended cycling with an upper cutoff potential of 0.65 V. At first glance, the flatter initial slope of the accumulated irreversible capacity within the first 60 cycles under delithiation-limited conditions (see marine symbols in Figure 3) suggests that the extent of silicon particle expansion may be reduced under these conditions. Hence, Figure 5c shows the HAADF image and the EDS spectra for the silicon-graphite electrodes after 60 cycles between 0.01–0.65 V vs. $Li^+$/Li. Analogous to the electrodes that were fully (de-)lithiated (compare Figure 5b), the delithiation-limited silicon particles reveal the same formation of a continuous network consisting of nanometer-sized silicon branches, which indicates that the investigated silicon particles undergo the same dealloying reactions, despite the lesser degree of delithiation at this lower cutoff potential. No significant differences could be observed for the two cutoff conditions during several repeat measurements after 60 cycles (compare Figures 5b and 5c) as well as after 40 cycles (data not shown), which demonstrates that the here investigated upper cutoff potentials do not affect the extent of the permanent silicon particle expansion. This demonstrates that a residual amount of about ~15% active lithium at 0.65 V upper cutoff potential (in contrast to essentially 0% for an upper cutoff potential of 1.25 V) does not prevent the morphological changes of the silicon particles caused by the dealloying mechanism. As a result, the flatter slope of the accumulated irreversible capacity loss curve for the delithiation-limited cycling procedure shown in Figure 3 cannot be explained by differences in silicon particle expansion and the concomitant formation of additional surface area. Instead, there must exist another reason for the differences in the total irreversible capacity curve within the first 60 cycles, which is related to the cutoff potentials and explains why the slope for the delithiation-limited cycling is already lower over the initial ~60 cycles (compare Figure 3).

In order to explain this apparent discrepancy, we propose that this phenomenon is related to the differences in the relative surface area change of the silicon particles, $\Delta S_{Si}/S_{Si,0}$, with $\Delta S_{Si}$ being the surface area differences between the lower and the upper cutoff potential, and with $S_{Si,0}$ being the surface area at the upper cutoff potential (i.e., at the lowest degree of lithiation). This is because the relative change in silicon surface area over the course of one lithiation/delithiation cycle should be directly proportional to the in-plane mechanical stress on the SEI layer at the silicon surface and, in turn, to the extent of the SEI cracking and re-formation.[8] In other words, although the total surface area of the silicon particles is continuously increasing as a consequence of the above described morphological changes, the repeated volume changes upon (de-)lithiation over the course of every single lithiation/delithiation presents an additional irreversible capacity contribution. It is known from the literature that silicon particles expand almost linearly as a function of the lithium content.[52] However, based on simple geometric considerations of the volume-surface relation of a sphere, which are shown in Figure 7a, it can be demonstrated that the concomitant increase of the surface area (see dotted red line) of a sphere is larger during the initial stages of lithiation (indicated by the steeper slope of the dotted read line for small x-values) compared to the lower relative increase of the surface area at higher degrees of lithiation (reflected by the lower slope at high x-values). While our silicon particles are clearly not spherical, we are using this analysis based on spherical particles as a zero-order approximation to describe the processes occurring at the silicon/electrolyte interface. The goal is merely to demonstrate based on simple geometric considerations that depending on the degree of lithiation the relative surface area changes of silicon vary in their extent. This has an important implication on the in-plane mechanical stress on the SEI layer and thus the resulting coulombic efficiency. As the extent of the differences depends

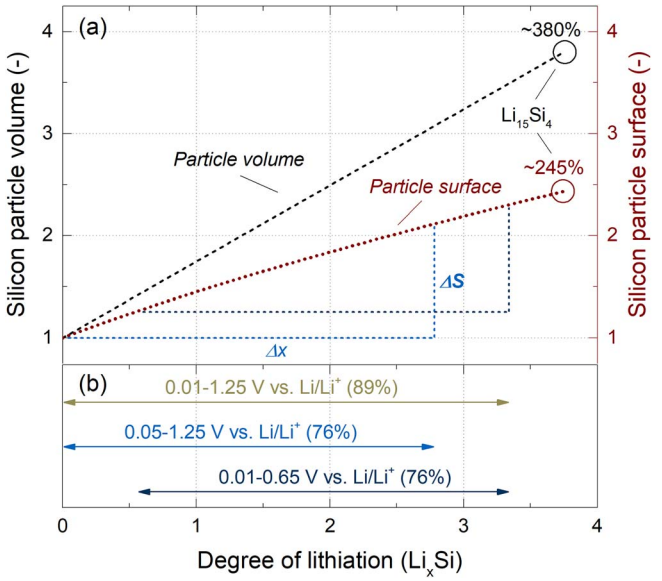


**Figure 7.** Illustration of (a) the relative volume $V_{Si,rel} \equiv V_{LixSi}/V_{si}$ (dashed black line, left axis) and the relative surface area $S_{Si,rel} \equiv S_{LixSi}/S_{si}$ (dotted red line, right axis) of a spherical silicon nanoparticle as a function of the degree of lithiation $x$ in $Li_xSi$. b) Initial degree of lithiation ranges for the three investigated cutoff conditions, which were calculated based on their reversible capacity at 0.33 $h^{-1}$ as obtained from the constant current cycling shown in Figure 2b. The blue and the marine dashed triangles represent the surface area changes for the lithiation- and delithiation-limited cutoff conditions, respectively.

strongly on the morphology of the silicon active material (as well as their changes upon cycling), this will not enable a prediction of the exact values of $\Delta S_{Si}$ during lithiation/delithiation. Yet, we think that it will allow a semi-quantitative assessment of the different behavior of silicon depending on the applied cutoff potentials.

Based on the initial capacities of the SiG electrodes at 0.33 $h^{-1}$ (see Figure 2b) and under the assumption of the same theoretical capacity utilization for silicon and graphite (i.e., ~89% at 0.01–1.25 V), the range of the degrees of lithiation $x$ (referring to $Li_xSi$) of the silicon particles for the different cycling protocols can be estimated and is indicated in Figure 7b: (i) x ≈ 0–3.34 for the deep (de-)lithiation cycling (0.01–1.25 V cutoff potentials); (ii) x ≈ 0–2.85 for lithiation-limited cycling (0.05–1.25 V cutoff potentials); and, (iii) x ≈ 0.49–3.34 for the delithiation-limited cycling (0.01–0.65 V cutoff potentials). Upon continued cycling, the ranges of the degree of lithiation change, because of the capacity fade and disconnection of silicon particles. Therefore, the total volume expansion and the total surface area will also decrease, resulting in a lower capacity fade upon extended cycling across all cutoff potentials (see Figure 2b). Nonetheless, at least over the first 20–30 cycles, i.e., during the period of the largest degradation (see Figure 3), these changes are reasonably small, which allows a fair comparison of the different degree of lithiation ranges. While, the surface area of conceptual silicon spheres over a lithiation-limited (blue arrow in Figure 7b) and a deep (de-)lithiation cycle (brown arrow) changes by ~113% (derived from $\frac{S_{Si,rel\ (x=2.85)}}{S_{Si,rel\ (x=0)}} - 1 = \frac{2.13}{1} - 1$) and ~128% (froam $\frac{S_{Si,rel\ (x=3.34)}}{S_{Si,rel\ (x=0)}} - 1 = \frac{2.28}{1} - 1$), respectively, the silicon particle surface area over a delithiation-limited cycle (see marine arrow) changes by only ~82% (from $\frac{S_{Si,rel\ (x=3.34)}}{S_{Si,rel\ (x=0.49)}} - 1 = \frac{2.28}{1.25} - 1$). Normalizing these values to the number of inserted/extracted lithium atoms $x$ (as defined by $Li_xSi$) per half-cycle reveals that the delithiation-limited silicon experiences a relative surface area change of ~30% per exchanged lithium atom (i.e., ~82% divided by $\Delta x = 2.85$), whereas the lithiation-limited (i.e., ~113% divided by $\Delta x = 2.85$) and the fully (de-)lithiated electrodes (i.e., ~128% divided by $\Delta x = 3.34$) experience almost the same but notably higher relative surface area change of 38–40% per lithium atom. Considering that a larger relative change in the silicon surface area during a (de-)lithiation cycle should lead to increased cracking and renewal of the SEI on the silicon surface, the results from this admittedly rather rough estimate of relative surface area changes for hypothetical silicon spheres provide a feasible explanation for the lower slope in the initial total irreversible capacity gain of the delithiation-limited cycling (see Figure 3) compared to cycling to full delithiation.

In summary, the initially high slope of the total irreversible capacity curves (Figure 3) is largely governed by the formation of nanoporous silicon particles with increasingly higher surface area, whereby this morphology evolution is not significantly affected by the here examined cutoff potentials (see Figure 5). The more subtle differences in the initial slopes are likely due to the above described relative surface area changes over a lithiation/delithiation cycle depending on the cutoff voltages. After an extended number of cycles, quasi steady-state silicon nanostructures are obtained and the flatter slope of the total irreversible capacity curves seems to be mostly controlled by the relative silicon surface area changes per cycle. The observed similar slopes for all cycling protocols suggest that the higher remaining capacity of the delithiation-limited cycled electrodes compensates for its lower value of relative surface area change per exchanged capacity. As a corollary, the silicon particle degradation can be considered as the root cause for the aging of SiG electrodes and an intrinsic property of the silicon particles. The underlying dealloying reactions likely depend on the initial size and shape of the silicon particles as well as their chemical composition (e.g., oxygen content). Although the dealloying induced roughening of the here studied silicon particles is almost independent of the chosen cutoff potentials (within the range studied here), it is conceivable that different particle morphologies, the use of active-inactive alloys, and a significantly reduced capacity utilization may help to mitigate the extent of this phenomenon. For example, Krause et al.[56] reported in a recent publication a very stable BET surface area over 80 cycles for silicon-graphite electrodes, featuring 15 wt% of ~5 μm particles of a silicon alloy. In these alloys, nano-domains of silicon are immersed in an alloy matrix which suppresses the morphological changes of silicon and decreases the surface area exposed to the electrolyte.[43]

***Electrode degradation upon repeated (de-)lithiation.—***While the coulombic efficiency of the SiG electrodes shown in Figure 2a is largely determined by the morphological changes of the silicon nanoparticles and subsequent electrolyte decomposition, the discrepancy in the cycling stability (see Figure 2b) at the different cutoff potentials requires to consider the entire electrode structure.[39] Figure 8 shows the differential capacity curves of the SiG electrodes of the 5th, 20th, 40th, and 60th cycle for the different cutoff potentials. The electrodes that were delithiated to 1.25 V vs. $Li^+/Li$ (panel a and b) reveal a severe capacity decay at low degrees of lithiation (i.e., at high potentials), whereas the delithiation-limited electrode (panel c) indicates only a minor fading. From previous studies it is known that the distinct potential drop to 0.2 V vs. $Li^+/Li$ at the beginning of lithiation (see Figures 8a and 8b) is mainly caused by an incomplete delithiation from the silicon nanoparticles during the preceding cycle, which is reflected by the disappearance of the delithiation capacity contribution at potentials above 0.55 V vs. $Li^+/Li$.[15,39] Further, it can be seen in panel a) and b) that the nominally fully delithiated electrodes show an increasingly growing polarization of the (de-)lithiation from silicon during lithiation at ~0.15 V vs. $Li^+/Li$ as well as during delithiation at ~0.35 V vs. $Li^+/Li$, indicating higher charge transfer overpotentials and resulting in an additional capacity loss. Again, this behavior is notably less pronounced for delithiation-limited cycling of silicon (see Figure 8c). The discrepancy in the electrode polarization is in good agreement with the SiG electrode impedances at the different cutoff potentials, which are shown in Figure 9. After formation, i.e., before switching to the individual cutoff potential ranges, all electrodes reveal a distorted semicircle with a similar overall impedance of ~2.4 Ω $cm^2$. The values were extracted from the Nyquist plot shown in the insert in Figure 9, by fitting with two R/Q elements which cor-

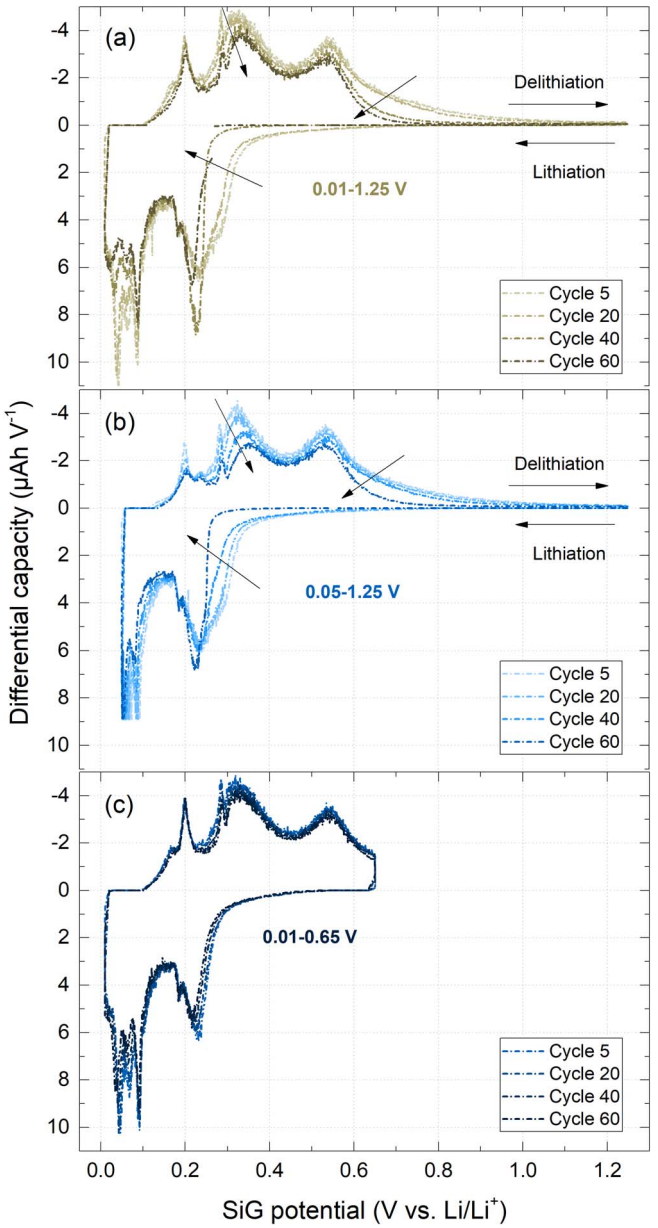


**Figure 8.** Differential capacity curves of selected cycles, obtained from constant current cycling (0.33 $h^{-1}$) of SiG//LFP Swagelok T-cells at different cutoff potentials: 0.01–1.25 V vs. $Li^+$/Li(brown), 0.05–1.25 V vs. $Li^+$/Li (blue), and 0.01–0.65 V vs. $Li^+$/Li (marine). These plots are derived from the measurements shown in Figure 2.

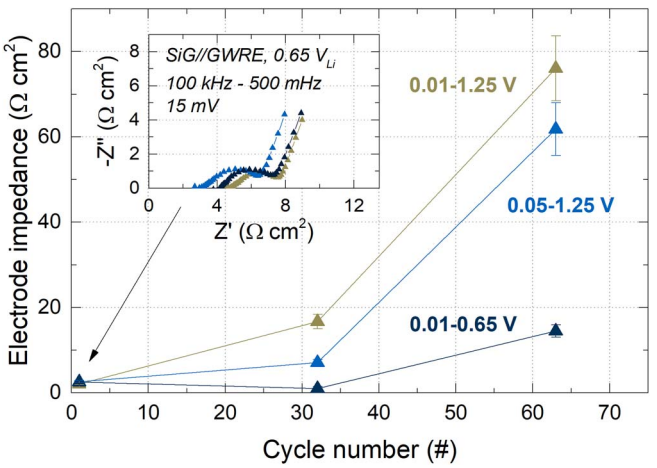


**Figure 9.** Electrode impedance of the silicon-graphite electrodes as a function of the cycle number, obtained at several cycles during the constant current cycling of SiG//LFP Swagelok T-cells at different cutoff potentials: 0.01–1.25 V vs. $Li^+$/Li(brown), 0.05–1.25 V vs. $Li^+$/Li (blue), and 0.01–0.65 V vs. $Li^+$/Li (marine). Potentiostatic impedance spectroscopy was measured at 0.65 V vs. $Li^+$/Li after a 30 min constant voltage step during the delithiation of the intermediate cycles at low currents (0.02 $h^{-1}$). Perturbation 15 mV, frequency range: 100 kHz – 500 mHz, temperature: 25°C. Insert: Nyquist spectra of the silicon-graphite electrodes during the 1st cycle after formation.

respond to the charge-transfer and the initial SEI layer on the active materials.[57] After 60 cycles, however, the two electrodes that were fully delithiated to 1.25 V vs. $Li^+$/Li (brown and blue symbols) show a significant impedance increase up to ~62 Ω $cm^2$ and ~76 Ω $cm^2$, respectively. At the same time, the delithiation-limited electrode reveals only a small increase up to ~14 Ω $cm^2$, which supports the lower polarization shown in the differential capacity analysis and agrees with a better silicon particle connectivity as indicated by the higher capacity retention shown in Figure 2b.

To examine whether there are any changes in electrode morphology which could be ascribed to the differences in the cycling stability and electrode impedance as a function of cutoff potentials, Figure 10 shows representative cross-sectional scanning electron microscopy (SEM) images of (a) an uncycled silicon-graphite electrode, as well as after 60 cycles (b) at full (de-)lithiation (0.01–1.25 V), and (c) at the delithiation-limited conditions (0.01–0.65 V). While in the uncycled electrode the well dispersed silicon nanoparticles and the flake-like graphite particles can be distinguished easily, the two cycled electrodes are largely filled by electrolyte decomposition products that penetrate a large share of the pores and additionally cover the active material particles. In agreement with the STEM-EDS analysis of cycled silicon particles shown in Figure 5, the original silicon nanoparticles can be barely identified in panels b) and c). Instead, a variety of differently sized agglomerates can be seen (see white arrow in Figure 10b), likely resulting from the expansion of the silicon particles and subsequent formation of large continuous networks of nanometer-sized silicon branches, which are extensively penetrated by SEI precipitates. Furthermore, the graphite particles are no longer predominantly aligned parallel to the current collector surface, but rather display random orientations across the electrode thickness, which in principle could originate from a substantial expansion of the electrode in a direction normal to the current collector surface, driven, e.g., by the large expansion of the silicon particles. A visual comparison of the SEM cross sections of the electrodes which were cycled under delithiation-limited conditions (Figure 10c) versus under conditions of full (de-)lithiation (Figure 10b) indicates that the SEI precipitates of the former are still more macro-porous and less agglomerated in feature size compared to the latter, which is in line with the improved cycling stability (see Figure 2b and Figure 8) of the electrodes cycled under delithiation limited conditions.

In order to describe the morphological changes between these electrodes more quantitatively, we determined the thickness of the coatings after 60 cycles between the different cutoff potentials and compared it to the uncycled electrodes, which is shown in Figure 11. Accordingly, the SiG electrodes that were fully (de-)lithiated upon cycling reveal a considerable thickness increase of +163% from ~18 to ~45 μm after 60 cycles, at which point the total irreversible capacity amounts to 1.79 mAh $cm^{-2}$ (see Figure 3). Similarly, the lithiation-limited electrodes, which over the course of 60 cycles remains at a ~15% lower delithiation capacity (Figure 2b) and accumulates a somewhat lower irreversible capacity up to this point (1.63 mAh $cm^{-2}$, see Figure 3), still shows an increase of +143% to 41 μm. The by fare lowest increase of electrode thickness is observed for the delithiation-limited electrode (+98% to 34 μm), which is in line with its lowest total irreversible capacity after 60 cycles (1.24 mAh $cm^{-2}$, see

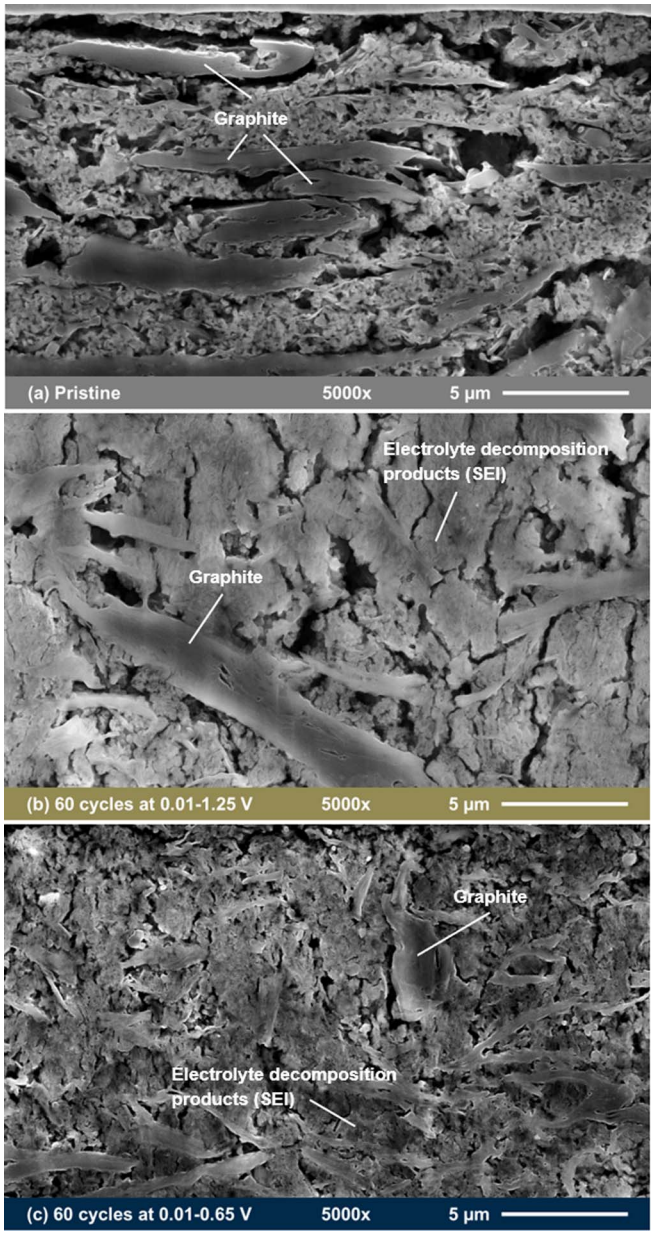


**Figure 10.** Scanning electron microscopy (SEM) cross-sectional images of (a) an uncycled electrode, (b) after 60 cycles between 0.01–1.25 V vs. $Li^+$/Li, and (c) after 60 cycles between 0.01–0.65 V vs. $Li^+$/Li. SEM specifications: secondary electron detector (SE), 10.0 kV electron acceleration voltage, magnification x5,000. Cross-sections were prepared with an Ar-ion beam cross-section polisher and the horizontal direction of the images is parallel to the current collector surface.

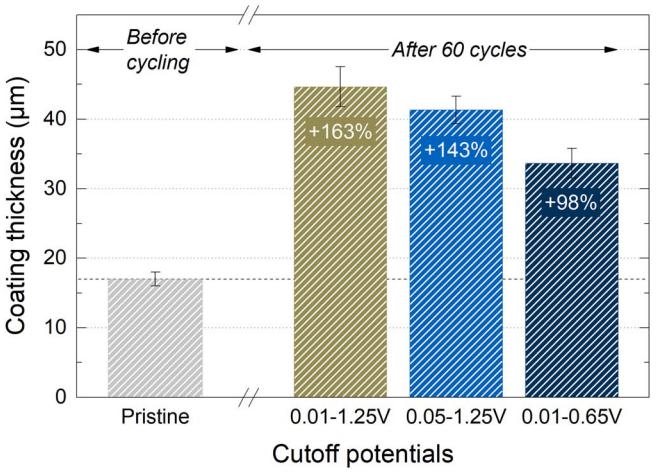


**Figure 11.** Silicon-graphite electrode coating thickness in pristine state and after 60 cycles, obtained from constant current cycling (0.33 $h^{-1}$) of SiG//LFP Swagelok T-cells at different cutoff potentials: 0.01–1.25 V vs. $Li^+$/Li(brown), 0.05–1.25 V vs. $Li^+$/Li (blue), and 0.01–0.65 V vs. $Li^+$/Li (marine).

Figure 3), despite the fact that the total exchanged charge+discharge capacity at this point is in between that of the electrodes which underwent lithiation-limited and deep (de-)lithiation cycling (see Figure 3). To further examine these trends, it is instructive to determine whether the amount of SEI products formed can be related directly to the gain in electrode thickness, i.e., whether the electrode thickness gain is directly proportional to the total irreversible capacity: (i) $\sim 15\ \mu m_{\Delta t}\ (mAh_{\Sigma Qirr}\ cm^{-2})^{-1}$ for the deep (de-)lithiation cycling, (ii) $\sim 15\ \mu m_{\Delta t}\ (mAh_{\Sigma Qirr}\ cm^{-2})^{-1}$ for lithiation-limited cycling, and (iii) $\sim 13\ \mu m_{\Delta t}\ (mAh_{\Sigma Qirr}\ cm^{-2})^{-1}$ for the delithiation-limited cycling. The approximately constant value of $\mu m_{\Delta t}\ (mAh_{\Sigma Qirr}\ cm^{-2})^{-1}$ indicates that there is a good correlation between thickness gain and total irreversible capacity, which suggests that the electrode thickness expansion by the formation of porous silicon nanostructures has approximately the same contribution for all cycling protocols (which is consistent with Figure 5), and that the buildup of SEI does not only occur inside the silicon nanostructures but also on their outside, thus leading to the differences in thickness between the electrodes.

As a corollary, the electrode degradation can be considered as consequence of the silicon particle degradation, which additionally depends on the electrode composition, including its electrical conductivity and mechanical integrity.[39] For that reason, we observe a very similar degradation for the fully (de-)lithiated and the lithiation-limited electrodes (both with an upper cutoff potential of 1.25 V), both in terms of electrode swelling and impedance increase, which causes the immobilization of lithium within the first 60 cycles and results in a similarly poor cycling stability. In contrast, the delithiation-limited electrode reveals a considerably smaller swelling and impedance increase, which mainly results from the smaller relative surface area changes and the consequently lower total amount of electrolyte decomposition products across the electrode coating. Therefore, the beneficial effect of a limited delithiation of silicon-based electrodes on the cycling stability is considerably larger compared to a limited lithiation, at least as long as the initial reversible capacity is kept constant for both conditions (here: ~1.45 mAh $cm^{-2}$, ~76%). Once the capacity utilization of the lithiation-limited protocol is reduced further, e.g., to 50%, it also decreases the irreversible capacity and eventually becomes on par with the delithiation-limited protocol, however, only at the expense either of a smaller reversible capacity or alternatively an oversized electrode.

Finally, we would like to note that although the delithiation-limited cycling of silicon-based electrodes is more favorable not only in terms of the cycling stability but also because of the lower average electrode potential and the full utilization of graphite, it also requires a higher initial investment of active lithium (here: ~0.25 mAh $cm^{-2}$) that needs to be provided either by a larger positive electrode or suitable prelithiation of the silicon-based electrode. Therefore, a comprehensive evaluation of this cycling protocol in practical lithium-ion full cells also requires a careful consideration of the electrode balancing and the effective energy density.

## Conclusions

In this study, we investigated the degradation of silicon-graphite electrodes with respect to the morphological changes of the silicon nanoparticles and the entire electrode structure in dependence on the applied cutoff potentials. Based on our recent classification of (i) the silicon particle degradation and (ii) the electrode degradation, we

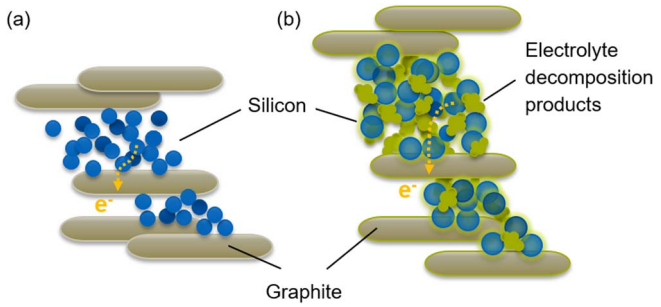


**Scheme 1.** Illustration of the difference in the mean electron conduction path length from individual silicon particles to the electrically conductive graphite particles in (a) an uncycled and (b) an aged silicon-graphite electrode.

summarized the underlying mechanisms as follows: Within the first 60 cycles, the silicon nanoparticles undergo severe morphological changes caused by dealloying reactions that result in (i) the expansion of initially solid silicon particles into porous networks of nanometer-sized silicon branches, (ii) a large concomitant increase of the silicon surface area which causes further SEI growth and leads to an increase of the irreversible capacity, and (iii) a significant volume expansion of the silicon particles not only reversibly over the course of a single lithiation/delithiation cycle but also permanently of up to +700% as indicated by STEM measurements. Driven by the increasing amount of electrolyte decomposition products and the volumetric changes of silicon, the SiG electrodes substantially increase in thickness during the same period, which we try to capture by Scheme 1. Both the insulating electrolyte decomposition products and the particle disconnection during electrode swelling result in a continuous impedance growth upon cycling that leads to an incomplete delithiation from electrically poorly connected silicon particles and thus to a distinct decay of the reversible capacity However, at some point the dealloying reactions reach a steady-state at which the silicon surface growth over cycling gradually diminishes.[39] At the same time, irreversible capacity losses and electrode swelling also approach a minimum after ~60 cycles, resulting in a stabilization of the reversible capacity with minor ongoing capacity fade. Although this degradation occurs in all investigated potential ranges, we conclude that the occurrence and the consequences can be delayed and reduced by limiting the delithiation of silicon to 0.65 V vs. $Li^+/Li$, which reduces the initially accessible capacity by ~15%, but owing to the lower capacity fade rate, the delithiation-limited cycling results in a superior absolute capacity after 40 cycles compared to the other cycling protocols. Our simplified theoretical consideration of a perfectly spherical silicon particle shows that by deliberately leaving ~15% of the reversible capacity in the particle, the relative surface area changes between end-of-lithiation and end-of-delithiation can be effectively reduced, thus mitigating the lateral stress at the particle surface and reducing SEI growth.

## Acknowledgments

The German Federal Ministry for Economic Affairs and Energy is acknowledged for funding (funding number 03ET6045D). S.S and D.P acknowledge BASF SE for funding through its Scientific Network on Electrochemistry and Batteries. The authors kindly acknowledge Dr. Sonja Gürster and Dr. Susanne Cornfine (both JEOL Germany GmbH) for the preparation and measurement of the cross-sectional SEM images. Wacker Chemie AG is kindly acknowledged for providing the silicon nanoparticles.

## ORCID

Morten Wetjen https://orcid.org/0000-0002-2357-1151
Sophie Solchenbach https://orcid.org/0000-0001-6517-8094
Daniel Pritzl https://orcid.org/0000-0002-9029-107X

## References

1. O. Gröger, H. A. Gasteiger, and J.-P. Suchsland, *J. Electrochem. Soc.*, **162**(14), A2605 (2015).
2. K. G. Gallagher, S. Goebel, T. Greszler, M. Mathias, W. Oelerich, D. Eroglu, and V. Srinivasan, *Energy Environ. Sci.*, **7**, 1555 (2014).
3. S.-T. Myung, F. Maglia, K.-J. Park, C. S. Yoon, P. Lamp, S.-J. Kim, and Y.-K. Sun, *ACS Energy Lett.*, **2**, 196 (2017).
4. C. J. Wen and R. A. Huggins, *J. Solid State Chem.*, **37**, 271 (1981).
5. R. N. Seefurth and R. A. Sharma, *J. Electrochem. Soc.*, **124**(8), 1207 (1974).
6. R. A. Sharma and R. N. Seefurth, *J. Electrochem. Soc.*, **123**(12), 1763 (1976).
7. M. N. Obrovac and L. Christensen, *Electrochem. Solid-State Lett.*, **7**(5), A93 (2004).
8. M. N. Obrovac and V. L. Chevrier, *Chem. Rev.*, **114**, 11444 (2014).
9. J. Christensen and J. Newman, *J. Solid State Chem.*, **10**, 293 (2006).
10. Z. Du, R. A. Dunlap, and M. N. Obrovac, *J. Electrochem. Soc.*, **161**(10), A1698 (2014).
11. B. Key, R. Bhattacharyya, M. Morcrette, V. Sezne, J. Tarascon, and C. P. Grey, *J. Am. Chem. Soc.*, **131**, 9239 (2009).
12. M. T. McDowell, S. W. Lee, J. T. Harris, B. A. Korgel, C. Wang, W. D. Nix, and Y. Cui, *Nano Lett.*, **13**, 758 (2013).
13. M. T. McDowell, S. W. Lee, W. D. Nix, and Y. Cui, *Adv. Mater.*, **25**, 4966 (2013).
14. M. N. Obrovac and L. J. Krause, *J. Electrochem. Soc.*, **154**(2), A103 (2007).
15. T. Yoon, C. C. Nguyen, D. M. Seo, and B. L. Lucht, *J. Electrochem. Soc.*, **162**(12), A2325 (2015).
16. D. S. M. Iaboni and M. N. Obrovac, *J. Electrochem. Soc.*, **163**(2), A255 (2016).
17. T. Kasukabe, H. Nishihara, S. Iwamura, and T. Kyotani, *J. Power Sources*, **319**, 99 (2016).
18. D. Ma, Z. Cao, and A. Hu, *Nano-Micro Lett.*, **6**(4), 347 (2014).
19. C. K. Chan, H. Peng, G. A. O. Liu, K. Mcilwrath, X. F. Zhang, R. A. Huggins, and Y. I. Cui, *Nat. Nanotechnol.*, **3**, 31 (2008).
20. M. T. McDowell, I. Ryu, S. W. Lee, C. Wang, W. D. Nix, and Y. Cui, *Adv. Mater.*, **24**, 6034 (2012).
21. U. Kasavajjula, C. Wang, and A. J. Appleby, *J. Power Sources*, **163**, 1003 (2007).
22. F. Béguin, F. Chevallier, C. Vix-Guterl, S. Saadallah, V. Bertagna, J. N. Rouzaud, and E. Frackowiak, *Carbon N. Y.*, **43**, 2160 (2005).
23. A. N. Dey, *J. Electrochem. Soc.*, **118**(10), 1547 (1971).
24. M. M. Nicholson, *J. Electrochem. Soc.*, **121**(6), 734 (1974).
25. A. M. Wilson and J. R. Dahn, *J. Electrochem. Soc.*, **142**(2), 326 (1995).
26. B. M. L. Rao, R. W. Francis, and H. A. Christopher, *J. Electrochem. Soc.*, **124**(10), 1490 (1977).
27. T. D. Hatchard and J. R. Dahn, *J. Electrochem. Soc.*, **151**(6), A838 (2004).
28. J. Li and J. R. Dahn, *J. Electrochem. Soc*, **154**(3), A156 (2007).
29. S. Tardif, E. Pavlenko, L. Quazuguel, M. Boniface, M. Maréchal, J. S. Micha, L. Gonon, V. Mareau, G. Gebel, P. Bayle-Guillemaud, F. Rieutord, and S. Lyonnard, *ACS Nano*, **11**, 11306 (2017).
30. X. Q. Yang, J. McBreen, W. S. Yoon, M. Yoshio, H. Wang, K. Fukuda, and T. Umeno, *Electrochem. commun.*, **4**, 893 (2002).
31. B. Key, M. Morcrette, J.-M. Tarascon, and C. P. Grey, *J. Am. Chem. Soc.*, **133**, 503 (2011).
32. Y. Oumellal, N. Delpuech, D. Mazouzi, N. Dupré, J. Gaubicher, P. Moreau, P. Soudan, B. Lestriez, and D. Guyomard, *J. Mater. Chem.*, **21**, 6201 (2011).
33. N. Delpuech, N. Dupre, P. Moreau, J. S. Bridel, J. Gaubicher, B. Lestriez, and D. Guyomard, *ChemSusChem*, **9**, 841 (2016).
34. A. L. Michan, G. Divitini, A. J. Pell, M. Leskes, C. Ducati, and C. P. Grey, *J. Am. Chem. Soc.*, **138**, 7918 (2016).
35. X. H. Liu, L. Zhong, S. Huang, S. X. Mao, T. Zhu, and J. Y. Huang, *ACS Nano*, **6**(2), 1522 (2012).
36. H. Wu, G. Chan, J. W. Choi, I. Ryu, Y. Yao, M. T. McDowell, S. W. Lee, A. Jackson, Y. Yang, L. Hu, and Y. Cui, *Nat. Nanotechnol.*, **7**, 310 (2012).
37. M. Nie, D. P. Abraham, Y. Chen, A. Bose, and B. L. Lucht, *J. Phys. Chem. C*, **117**, 13403 (2013).
38. X. H. Liu and J. Y. Huang, *Energy Environ. Sci.*, **4**, 3844 (2011).
39. M. Wetjen, D. Pritzl, R. Jung, S. Solchenbach, R. Ghadimi, and H. A. Gasteiger, *J. Electrochem. Soc.*, **164**(12), A2840 (2017).
40. E. Markevich, K. Fridman, R. Sharabi, R. Elazari, G. Salitra, H. E. Gottlieb, G. Gershinsky, A. Garsuch, G. Semrau, M. A. Schmidt, and D. Aurbach, *J. Electrochem. Soc.*, **160**(10), A1824 (2013).
41. M. Klett, J. A. Gilbert, K. Z. Pupek, S. E. Trask, and D. P. Abraham, *J. Electrochem. Soc.*, **164**(1), A6095 (2017).
42. K. Kimura, T. Matsumoto, H. Nishihara, T. Kasukabe, T. Kyotani, and H. Kobayashi, *J. Electrochem. Soc.*, **164**(6), A995 (2017).
43. V. L. Chevrier, L. Liu, D. B. Le, J. Lund, B. Molla, K. Reimer, L. J. Krause, L. D. Jensen, E. Figgemeier, and K. W. Eberman, *J. Electrochem. Soc.*, **161**(5), A783 (2014).
44. S. Solchenbach, D. Pritzl, E. J. Y. Kong, J. Landesfeind, and H. A. Gasteiger, *J. Electrochem. Soc.*, **163**(10), A2265 (2016).
45. T. Mittermeier, A. Weiß, F. Hasché, G. Hübner, and H. A. Gasteiger, *J. Electrochem. Soc.*, **164**(2), F127 (2017).
46. S. Solchenbach, M. Wetjen, D. Pritzl, K. U. Schwenke, and H. A. Gasteiger, *J. Electrochem. Soc.*, **165**(3), 512 (2018).
47. S. E. Trask, K. Z. Pupek, J. A. Gilbert, M. Klett, B. J. Polzin, A. N. Jansen, and D. P. Abraham, *J. Electrochem. Soc.*, **163**(3), A345 (2016).
48. R. Jung, M. Metzger, D. Haering, S. Solchenbach, C. Marino, N. Tsiouvaras, C. Stinner, and H. A. Gasteiger, *J. Electrochem. Soc.*, **163**(8), A1705 (2016).

49. Q. Chen and K. Sieradzki, *Nat. Mater.*, **12**, 1102 (2013).
50. J. Erlebacher, M. J. Aziz, A. Karma, N. Dimitrov, and K. Sieradzki, *Nature*, **410**, 450 (2001).
51. H. W. Pickering, *Corros. Sci.*, **23**, 1107 (1983).
52. L. Y. Beaulieu, T. D. Hatchard, A. Bonakdarpour, M. D. Fleischauer, and J. R. Dahn, *J. Electrochem. Soc.*, **150**(11), A1457 (2003).
53. I. McCue, E. Benn, B. Gaskey, and J. Erlebacher, *Annu. Rev. Mater. Res.*, **46**, 263 (2016).
54. K. W. Schroder, H. Celio, L. J. Webb, and K. J. Stevenson, *J. Phys. Chem. C*, **116**, 19737 (2012).
55. K. Schroder, J. Alvarado, T. A. Yersak, J. Li, N. Dudney, L. J. Webb, Y. S. Meng, and K. J. Stevenson, *Chem. Mater.*, **27**, 5531 (2015).
56. L. J. Krause, T. Brandt, V. L. Chevrier, and L. D. Jensen, *J. Electrochem. Soc.*, **164**(9), A2277 (2017).
57. M. Wetjen, G. Hong, S. Solchenbach, D. Pritzl, and H. A. Gasteiger, (2018), in preparation.